AGU PUBLICATIONS

Geochemistry, Geophysics, Geosystems

TECHNICAL REPORTS: DATA

10.1002/2016GC006397

Key Points:
- Abundant zircon in sepiolite drilling mud used in scientific drilling can contaminate rock samples
- Contaminating zircon grains may yield diverse and spurious ages and compositions

Supporting Information:
- Supporting Information S1

Correspondence to:
G. D. M. Andrews,
graham.andrews@mail.wvu.edu

Citation:
Andrews, G. D. M., A. K. Schmitt, C. J. Busby, S. R. Brown, P. Blum, and J. C. Harvey (2016), Age and compositional data of zircon from sepiolite drilling mud to identify contamination of ocean drilling samples, *Geochem. Geophys. Geosyst.*, *17*, 3512–3526, doi:10.1002/2016GC006397.

Received 12 APR 2016
Accepted 12 JUL 2016
Accepted article online 15 JUL 2016
Published online 27 AUG 2016

© 2016. American Geophysical Union. All Rights Reserved.

Age and compositional data of zircon from sepiolite drilling mud to identify contamination of ocean drilling samples

Graham D. M. Andrews[1,2], Axel K. Schmitt[3], Cathy J. Busby[4], Sarah R. Brown[2], Peter Blum[5], and Janet. C. Harvey[3]

[1]Department of Geology and Geography, West Virginia University, Morgantown, West Virginia, USA, [2]Department of Geological Sciences, California State University Bakersfield, Bakersfield, California, USA, [3]Institut für Geowissenschaften, Universität Heidelberg, Heidelberg, Germany, [4]Department of Earth and Planetary Sciences, University of California Davis, Davis, California, USA, [5]International Ocean Discovery Program, Texas A&M University, College Station, Texas, USA

Abstract Zircon extracted from drilled oceanic rocks is increasingly used to answer geologic questions related to igneous and sedimentary sequences. Recent zircon studies using samples obtained from marine drill cores revealed that drilling muds used in the coring process may contaminate the samples. The JOIDES Resolution Science Operator of the International Ocean Discovery Program has been using two types of clays, sepiolite and attapulgite, which both have salt water viscosifier properties able to create a gel-like slurry that carries drill cuttings out of the holes several hundred meters deep. The dominantly used drilling mud is sepiolite originating from southwestern Nevada, USA. This sepiolite contains abundant zircon crystals with U-Pb ages ranging from 1.89 to 2889 Ma and continental trace element, δ^{18}O, and εHf isotopic compositions. A dominant population of 11–16 Ma zircons in sepiolite drilling mud makes identification of contamination in drilled Neogene successions particularly challenging. Interpretation of zircon analyses related to ocean drilling should be cautious of zircon ages in violation of independently constrained age models and that have age populations overlapping those in the sepiolite. Because individual geochronologic and geochemical characteristics lack absolute discriminatory power, it is recommended to comprehensively analyze all dated zircon crystals from cores exposed to drill mud for trace element, δ^{18}O, and εHf isotopic compositions. Zircon analyzed in situ (i.e., in petrographic sections) are assumed to be trustworthy.

1. Introduction

The International Ocean Discovery Program (IODP; since 2013) and its predecessors (DSDP, Deep Sea Drilling Program 1966–1985; ODP, Ocean Drilling Program; 1985–2003; IODP, Integrated Ocean Drilling Program 2003–2013) use shipboard drilling techniques to collect sediment and rocks from the seafloor and subsurface [*Huey*, 2009; http://iodp.tamu.edu/tools/]. Zircon extracted from drilled oceanic successions increasingly becomes the mineral of choice to investigate the timing of igneous basement accretion and cooling [e.g., *Schwartz et al.*, 2005], seawater-rock interaction and magmatic differentiation of oceanic crust [e.g., *Grimes et al.*, 2011] or to resolve siliciclastic sediment provenance [e.g., *Clift et al.*, 2013; *Shinjoe et al.*, 2014]. It is therefore crucial that the scientific community is confident in the fidelity of the zircon record collected during IODP expeditions. This report alerts the geology community to the possibility that core samples may become contaminated during drilling with zircons derived from drilling mud. To aid in the identification of such contamination, we comprehensively characterized zircon derived from Sea Mud™ (sepiolite), currently the drilling mud used most frequently in activities of the JOIDES Resolution Science Operator (JRSO).

The authors know of no previous studies of zircon in drilling mud nor explicit discussion of zircon contamination in previous studies of cored samples. However, in the course of extracting zircon from volcanic intervals cored during IODP expeditions 350 (Site U1437) [*Andrews et al.*, 2015] and 352 (Site U1439) (Y. Li, Institute of Geology, Chinese Academy of Geological Science, personal communication, 2016), several processed samples yielded zircon much older than age expectations based on stratigraphic position, and magneto- and biostratigraphic markers. Low zircon yields (typically <5 zircons per interval) are common to both of these studies and this may be an important factor why contamination is only being recognized now for the first time, i.e., contaminating zircons are likely to be extremely diluted in samples with abundant zircons.

Samples with abundant zircon may still contain drilling mud contamination, and this may be difficult to detect by age alone in sedimentary rocks with diverse detrital zircon populations.

2. Background

2.1. Drilling Techniques and Disturbances

Shipboard drilling techniques involves recovery of oozes and soft sediments using the Advanced Piston Corer (APC) and Half-Length Advanced Piston Corer (HLAPC) whereas incipiently lithified sediment and hard-rocks require rotary coring by Extended Core Barrel (XCB) and Rotary Core Barrel (RCB) coring systems [*Graber et al*., 2002; *Huey*, 2009]. In riser-less drilling with the R/V JOIDES Resolution (JR), seawater is pumped from the surface through the drill pipe to cool the bit and to flush out cuttings. When coring with the APC and HLAPC, the seawater mixes with the material from the formation to create a slurry capable of carrying the cuttings out of the hole. RCB, XCB, and in some cases (e.g., with sandy layers or at depths at or beyond 300 mbsf) HLAPC coring, requires pumping "mud" into the borehole to create the slurry necessary to clean the hole during core cutting, or as intermittent mud sweeps. Contamination by mud is therefore most likely in holes after they have been swept-out.

Coring physically disturbs the recovered core and can expose sediment and rock to drilling fluids ("intrusion"). Intrusion of mud into core samples and noncased hole margins is likely to be greater when the lithologies are unlithified, porous, or heavily fractured. Moreover, drilling of heavily fractured intervals often leads to significant reductions in the volume of core recovered, often necessitating a change in drill-bit and a mud sweep. The mud is unlikely to be fully expelled during a sweep and may be ponded around the base of the hole or accreted to the margins when drilling resumes. In addition, "fall-in" of rock and sediment higher in the hole [e.g., *Jutzeler et al*., 2014] may repeatedly add mud that was accreted to the hole's margins or partially intruded into shallower, porous intervals. It is then possible that unexpelled mud is in contact with sample core during renewed drilling, and mechanical processes can forcibly propel mud into the core due to either the elevated water pressure or brittle-ductile deformation of the core (e.g., fracturing, brecciation, "biscuiting") [*Kidd*, 1978; *Leggett*, 1982].

2.2. Drilling Muds

Up to ODP Leg 154 (1992), bentonite was used exclusively to prepare drilling mud on the JR. Bentonite continued to be used up to IODP Expedition 306. Bentonite has to be mixed with fresh water to create a gel-like slurry. Therefore, starting with ODP Leg 155, use of sepiolite became more common. Sepiolite, a magnesium silicate with the chemical formula $Mg_4Si_6O_{15}(OH)_2{\cdot}6H_2O$, is a saltwater viscosifier which forms a gel with seawater able to carry heavier particles out of the hole. The sepiolite most commonly used on the JR is Sea Mud™. This sepiolite is quarried in the Amargosa Basin, Nye County, Nevada (Figure 1; 36°27.00′N and 116°28.11′N) [*Hosterman and Patterson*, 1992] by Industrial Mineral Ventures (IMV) Nevada, a division of Lhoist North America, which has been mining and processing specialty clays in the Amargosa Basin since 1972 [http://www.lhoist.com/us_en/imv-nevada]. JRSO has also employed attapulgite, also known as palygorskite, intermittently and interchangeably with sepiolite since Expedition 301. In addition, barite can be admixed to the mud, but typically only during logging operations and to fill a hole after operations are concluded.

2.3. Previous Studies of Drilling Fluid Contamination

Contamination assessments by lacing drilling fluids with synthetic chemical (perfluorocarbon tracers, PFT) and ~0.5 μm diameter particulate tracers (fluorescent microsphere beads) have indicated that intrusion does occur in IODP drilling but that it is insufficient to undermine its utility for microbiological studies [*Smith et al*., 2000a]. PFT intrusion was greatest at the outer edge of the core and rapidly diminishes inward although it is still detectable in the center of the core, is slightly greater in clay than in fine sand, and is largely independent of depth [*House et al*., 2003; *Lever et al*., 2006; *Yanagawa et al*., 2013]. Intrusion was also more severe in XCB compared to APC cores [*House et al*., 2003]. Microsphere intrusion was not detected in the center of the either igneous or sedimentary cores [*Smith et al*., 2000b]. These studies have limited applicability to zircon, which is typically much larger (~10 to 100 of μm) than the microbiological tracers used previously.

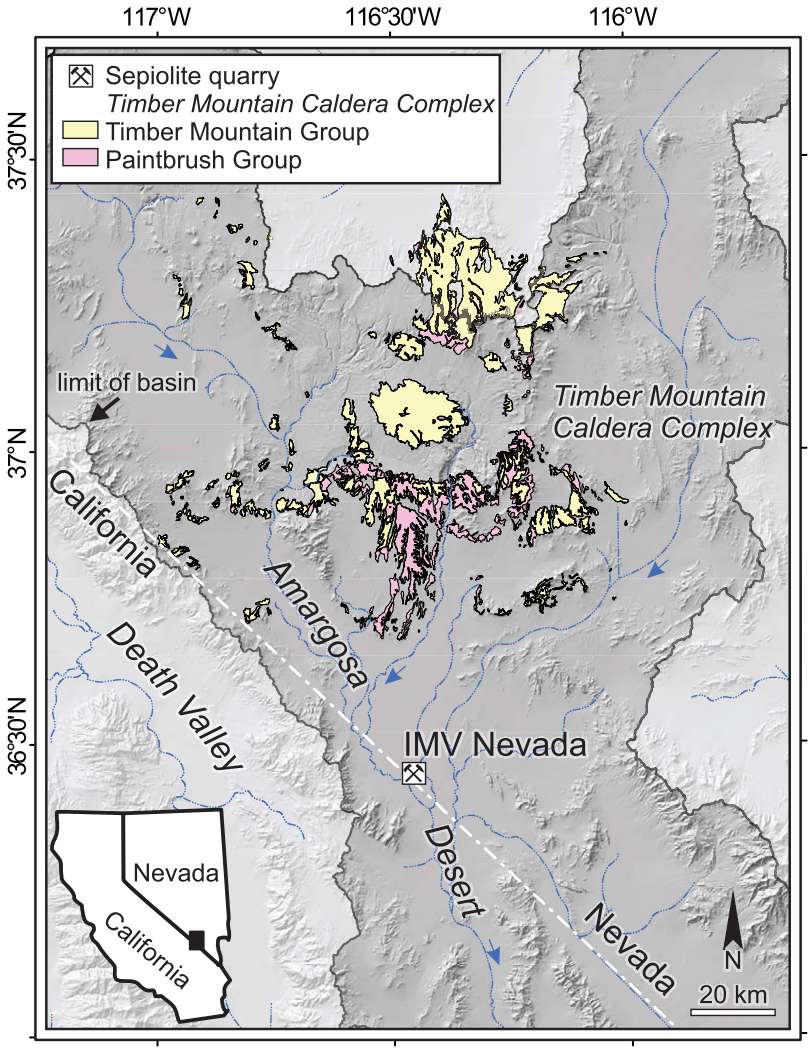

Figure 1. Location map of the IMV Nevada sepiolite quarry where Sea Mud™ originates. Map is based on the Shuttle Radar Topography Mission (SRTM) 30 m digital elevation model [*USGS*, 2006] with the major silicic volcanic deposits of the Timber Mountain Caldera Complex overlain [after *Minor et al.*, 1993; *Carr et al.*, 1996]. Hydrologic model for the upper Amargosa River basin was generated based on current topography from the finished SRTM dataset utilizing the ESRI ArcGIS spatial analyst hydrology toolset.

3. Methods

This report focuses on the presence of zircon in Sea Mud™. Comparable studies of attapulgite and barite drilling muds are in progress. Zircon crystals were separated from two 1 kg bags of dry Sea Mud™. Samples were prepared in a brand-new mineral separation facility at California State University Bakersfield featuring new or newly refurbished equipment and glassware; these samples were the first to be processed through the new lab. Samples were sieved to <250 μm, density sorted on a water (Wilfley™) table, magnetically separated, and density sorted in methelyene iodide (MEI; 3.32 g cm^{-3}). Zircon crystals where then hand-picked, mounted in epoxy, polished, gold-coated, and imaged by scanning electron microscopy with a cathodoluminescence detector (Figure 2; SEM-CL). A second batch of sepiolite was prepared similarly except that zircons were not hand-picked, and instead poured in an epoxy mount so as not to introduce bias before detrital geochronology analyses.

U-Pb geochronology, trace element, and oxygen isotope analysis of zircon followed established procedures for the CAMECA ims 1270 ion microprobe (or secondary ionization mass spectrometer SIMS) at UCLA (S1-3) [*Schmitt et al.*, 2003; *Monteleone et al.*, 2007; *Trail et al.*, 2007]. Reference zircons AS3 [*Paces and Miller*, 1993] and 91500 [*Wiedenbeck et al.*, 2004] were used. Hf isotopic compositions were determined at the Arizona LaserChron Center (S4) with a Nu laser ablation multicollector inductively coupled plasma mass spectrometry

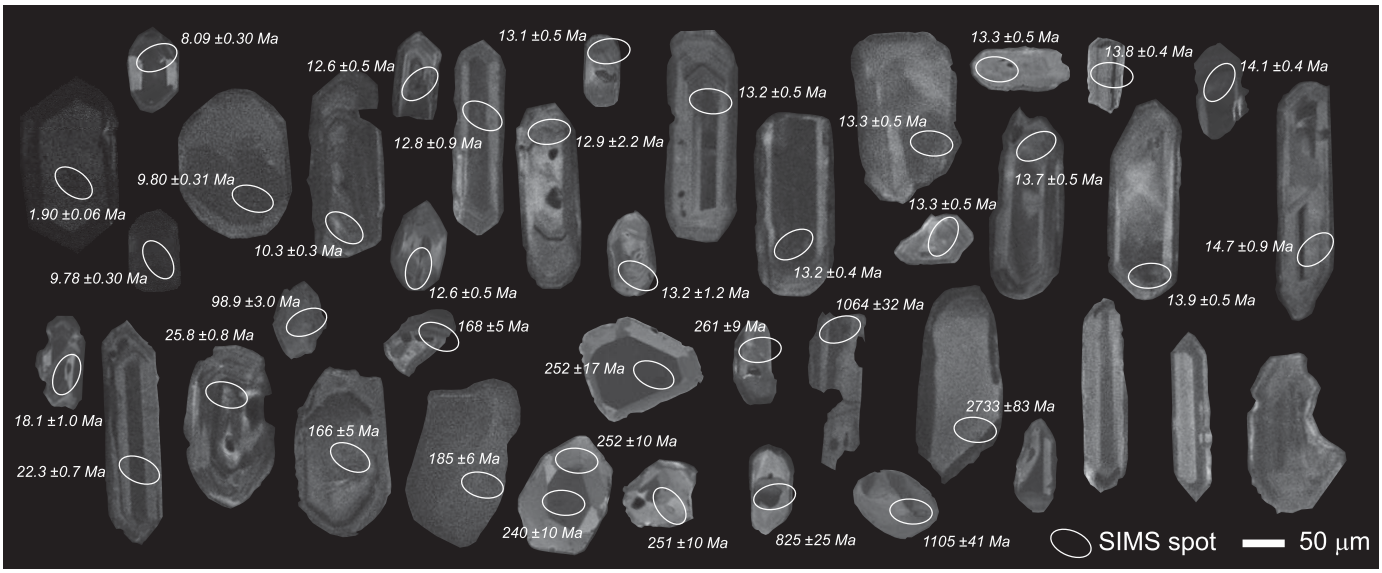

Figure 2. Cathodoluminescence images of sepiolite-derived zircons showing $^{206}Pb/^{238}U$ age ($\pm 1\sigma$) and SIMS spot position.

(LA-MC-ICP-MS) connected to a Photon Machines Analyte G2 excimer laser producing 40 μm spots centered on earlier SIMS pits [*Gehrels and Pecha*, 2014]. Reference zircons Mud Tank, 91500, Temora, R33, FC52, Plesovice, and Sri Lanka were analyzed. Long-term reproducibility of secondary reference materials (e.g., 91500 zircon) run under similar analytical conditions as in this study is equivalent to stated uncertainties (see supporting information). To more representatively sample the sepiolite age spectrum, U-Pb detrital zircon analyses by LA-MC-ICP-MS were also carried out at the Arizona LaserChron Center following established protocols (S5) [*Gehrels et al.*, 2008].

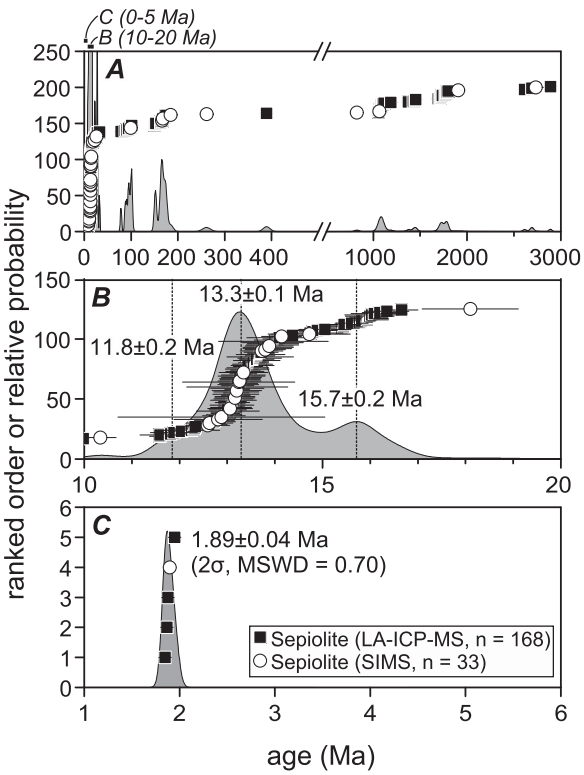

Figure 3. Ranked order and probability density plots for sepiolite detrital zircons analyzed by LA-ICP-MS and SIMS. Entire age range from (a) 0 to 3000 Ma, and subplots between (b) 10 and 20 Ma and (c) 0 and 5 Ma are shown. Dashed lines in Figure 3b correspond to subpopulations derived from the unmixing model of *Sambridge and Compston* [1994]; weighted average of the youngest zircon ages ($n = 5$) is stated (c). Middle Miocene and Quaternary $^{206}Pb/^{238}U$ zircon ages were corrected for initial disequilibrium in ^{230}Th.

4. Results

Zircon yields range between 10 and 100 s of grains per gram sepiolite. Grains are ~90–260 μm long, with variable morphology (54% stubby; 46% prismatic) and mostly (60%) euhedral to subhedral (Figure 2). Crystals are typically oscillatory-zoned or sector-zoned in SEM-CL (62%), but rare CL inactive (possibly metamict) grains occur (Figure 2). Mesozoic and older zircons are more likely to be anhedral. The presence of anhedral grains suggests some reworking, but their variability renders discrimination between sepiolite and target zircons according to size and morphology impractical.

Sepiolite zircon ages ($^{206}Pb/^{238}U$) span 1.89–2889 Ma ($n = 201$; Figure 3a; Tables 1 and 2), with an overwhelmingly prominent age peak at ca. 13 Ma (Figure 3b) and minor peaks at ca. 1.8 (Figure 3c), 27 Ma, 170 Ma, 250 Ma, 1.1 Ga, 1.8 Ga, and 2.7 Ga (Figure 3a). The complex age distribution indicates multiple

Table 1. U-Pb Geochronology Data Measured by SIMS

Zircon #	$^{206}Pb/^{238}U$[a] age (Ma)	$\pm 1\sigma$ $^{206}Pb/^{238}U$ age (Ma)	% radiogenic ^{206}Pb	$^{206}Pb/^{238}U$	$^{206}Pb/^{238}U$	$^{207}Pb/^{235}U$	$^{207}Pb/^{235}U$	$^{207}Pb/^{206}Pb$	$^{207}Pb/^{206}Pb$	Correlation of concordia ellipses	$^{204}Pb/^{206}Pb$	$^{204}Pb/^{206}Pb$	Th/U	U[b] ppm
5	1.90	0.06	97.45	0.00030	0.000008	0.00275	0.00013	0.06602	0.00281	0.457	0.00941	0.00124	0.15	2678.28
20	8.09	0.30	95.23	0.00132	0.000045	0.01517	0.00091	0.08349	0.00412	0.566	0.03090	0.00325	0.84	308.61
24	9.78	0.30	98.41	0.00154	0.000047	0.01247	0.00061	0.05866	0.00259	0.455	0.00806	0.00111	0.57	572.71
8	9.80	0.31	98.12	0.00155	0.000047	0.01303	0.00091	0.06098	0.00401	0.353	0.01004	0.00168	0.46	310.35
30	10.3	0.3	98.81	0.00162	0.000051	0.01243	0.00103	0.05554	0.00443	0.292	0.00175	0.00063	0.67	342.43
31	12.6	0.5	97.37	0.00201	0.000070	0.01850	0.00174	0.06684	0.00581	0.388	0.00649	0.00193	0.65	100.94
33	12.6	0.5	98.47	0.00199	0.000075	0.01601	0.00144	0.05829	0.00451	0.527	0.00362	0.00128	0.48	129.74
14	12.8	0.9	84.15	0.00236	0.000123	0.05549	0.00889	0.17020	0.02030	0.849	0.01644	0.00236	0.56	159.13
7	12.9	2.2	32.84	0.00609	0.000257	0.47970	0.02520	0.57150	0.01540	0.860	0.14430	0.00532	0.52	141.30
18	13.1	0.5	94.10	0.00216	0.000072	0.02746	0.00157	0.09241	0.00395	0.666	0.02419	0.00294	0.43	175.77
29	13.2	1.2	70.62	0.00291	0.000146	0.11080	0.01270	0.27610	0.01980	0.915	0.06125	0.00880	0.44	167.04
3	13.2	0.5	97.75	0.00210	0.000079	0.01848	0.00163	0.06391	0.00480	0.531	0.00705	0.00187	0.64	123.99
1	13.2	0.4	97.71	0.00209	0.000065	0.01850	0.00120	0.06417	0.00376	0.434	0.00808	0.00161	0.59	227.69
12	13.3	0.5	97.02	0.00212	0.000069	0.02036	0.00137	0.06960	0.00426	0.422	0.01480	0.00164	0.81	401.37
13	13.3	0.5	94.95	0.00218	0.000074	0.02573	0.00158	0.08580	0.00411	0.633	0.00786	0.00164	0.72	182.98
2	13.3	0.5	96.51	0.00215	0.000079	0.02178	0.00141	0.07356	0.00372	0.628	0.01217	0.00207	0.41	177.01
28	13.7	0.5	97.49	0.00219	0.000069	0.01987	0.00136	0.06595	0.00420	0.370	0.00385	0.00124	0.49	141.22
16	13.8	0.4	98.47	0.00218	0.000065	0.01749	0.00096	0.05831	0.00260	0.590	0.00625	0.00081	0.22	592.60
21	13.9	0.5	97.86	0.00220	0.000077	0.01914	0.00136	0.06301	0.00422	0.355	0.00615	0.00149	0.68	170.40
25	14.1	0.4	99.39	0.00221	0.000063	0.01557	0.00078	0.05113	0.00197	0.644	0.00241	0.00046	0.35	681.63
32	14.7	0.9	71.40	0.00320	0.000126	0.11920	0.00529	0.27000	0.00997	0.618	0.03984	0.00441	0.39	85.77
11	18.1	1.0	93.40	0.00301	0.000151	0.04070	0.00476	0.09804	0.00759	0.868	0.01451	0.00251	0.92	100.12
15	22.3	0.7	99.19	0.00349	0.000101	0.02540	0.00115	0.05277	0.00181	0.651	0.00265	0.00052	0.65	351.63
6	25.8	0.8	99.18	0.00405	0.000111	0.02957	0.00127	0.05295	0.00167	0.679	0.00854	0.00081	0.83	428.47
17	98.9	3.0	98.99	0.01562	0.000465	0.12030	0.00405	0.05585	0.00077	0.913	0.00115	0.00011	0.24	807.96
9	166	5	99.89	0.02612	0.000773	0.18090	0.00558	0.05022	0.00064	0.911	0.00038	0.00007	0.48	342.43
22	168	5	99.52	0.02652	0.000838	0.19450	0.00649	0.05320	0.00058	0.946	0.00183	0.00020	0.17	732.11
26	185	6	99.93	0.02907	0.000827	0.20170	0.00596	0.05030	0.00036	0.971	0.00023	0.00003	0.25	1196.89
19	261	9	99.76	0.04143	0.001400	0.30450	0.00991	0.05331	0.00066	0.930	0.00123	0.00012	0.18	399.13
23	825	25	98.91	0.13800	0.003610	1.42500	0.03670	0.07488	0.00027	0.991	0.00007	0.00001	0.42	557.29
4	1064	32	99.72	0.17990	0.005030	1.90800	0.05600	0.07693	0.00045	0.981	0.00024	0.00003	0.15	217.84
27	1904	57	101.00	0.34020	0.010700	5.11500	0.16300	0.10900	0.00039	0.994	0.00005	0.00001	0.38	465.03
10	2733	83	102.54	0.51490	0.019200	11.85000	0.44300	0.16690	0.00053	0.996	0.00008	0.00002	0.54	80.00

[a]Age after ^{207}Pb common Pb correction ($^{207}Pb/^{206}Pb = 0.8283$).
[b]Concentration from U-Pb analysis ($U^+/^{94}Zr_2O^+$ relative to 91500 reference zircon with 81 ppm U).

sources (see below). Their trace element compositions is equally heterogeneous (Table 3). Discrimination diagrams (Figure 4) indicate that sepiolite zircons have dominantly continental signatures, with only a few outliers in the mid-ocean ridge (MOR) field of *Grimes et al*. [2007, 2015]. Ti-in-zircon model temperatures calculated for activities of SiO_2 and $TiO_2 = 1$ [*Ferry and Watson*, 2007] range from 600 to 800°C with a mode at 725°C (Figure 4d). This is broadly equivalent to zircon from continental arc and continental rift-related mafic rocks (600–925°C, mode 700°C) [*Fu et al*., 2008], but mostly below the temperatures for zircons from MOR crustal rocks (625–1025°C, mode 750°C) [*Grimes et al*., 2009, 2015].

Oxygen isotope ratios ($\delta^{18}O$) vary from 4.34‰ to 9.77‰ (mode 7.00‰; Figure 4e). Thirteen zircons (35%) fall within the range of mantle $\delta^{18}O$ values (5.3 ± 0.6‰) of *Valley et al*. [2005] and MOR zircons (5.2 ± 0.5‰) of *Grimes et al*. [2011, 2013]. Like oxygen isotopes, sepiolite zircon $\varepsilon Hf_{(0)}$ (present-day) values are heterogeneous, but overwhelmingly at negative values which is not expected for oceanic crustal rocks with εHf values between +9 and +26 (Figure 4e). When calculating initial $\varepsilon Hf_{(t)}$ (Figure 4f) using the corresponding SIMS ages, the majority of sepiolite-derived zircons (88%) have continental affinity (negative $\varepsilon Hf_{(t)}$ values), with only a minor proportion of zircons being derived from largely mantle-derived magmas at the time of their crystallization. Depleted mantle model ages of ca. 1050–1700 Ma are typical of Proterozoic magmatic and orogenic events in the southwestern United States [e.g., *Gehrels and Pecha*, 2014].

5. Discussion

5.1. Sepiolite Zircon Provenance

Drainage analysis using digital elevation models [*USGS*, 2006] and published geologic maps [*Carr et al*., 1996; *Minor et al*., 1993] implicates the Timber Mountain caldera complex (TMCC, Figure 1) as the dominant

Table 2. U-Pb Detrital Zircon Age Data Measured by LA-MC-ICP-MS

				Isotope ratios							Apparent ages								
Analysis	U (ppm)	$^{206}Pb/^{204}Pb$	U/Th	$^{206}Pb^*/^{207}Pb^*$	± (%)	$^{207}Pb^*/^{235}Pb^*$	± (%)	$^{206}Pb^*/^{238}U$	± (%)	Error correlation	206Pb*/238U* (Ma)	±1σ (Ma)	207Pb*/235U (Ma)	±1σ (Ma)	206Pb*/207Pb* (Ma)	±1σ (Ma)	Best age (Ma)	±1σ (Ma)	Concordance (%)[a]
Sepiolite-Spot 14	2499	2334	2.9	17.3650	7.1	0.0022	7.4	0.0003	2.3	0.30	1.8	0.0	2.2	0.2	514.1	155.8	1.8	0.0	80.0
Sepiolite-Spot 27	3158	11206	2.9	18.3740	5.4	0.0021	5.9	0.0003	2.4	0.40	1.8	0.0	2.1	0.1	388.6	121.9	1.8	0.0	84.7
Sepiolite-Spot 15	1698	3024	2.5	18.0165	9.8	0.0021	10.2	0.0003	2.7	0.27	1.8	0.0	2.2	0.2	432.6	219.2	1.8	0.0	83.0
Sepiolite-Spot 23	5618	10412	3.7	18.7690	6.7	0.0021	7.1	0.0003	2.5	0.35	1.9	0.0	2.1	0.2	340.7	151.4	1.9	0.0	86.5
Sepiolite-Spot 3	121	5080	1.0	15.9565	16.0	0.0086	17.0	0.0010	5.6	0.33	6.4	0.4	8.7	1.5	697.1	343.0	6.4	0.4	73.8
Sepiolite-Spot 26	686	7142	0.5	19.6284	6.8	0.0082	7.4	0.0012	3.0	0.40	7.5	0.2	8.3	0.6	238.4	155.8	7.5	0.2	90.7
Sepiolite-Spot 42	356	36229	1.1	17.5135	9.4	0.0096	10.1	0.0012	3.6	0.36	7.9	0.3	9.7	1.0	495.4	208.6	7.9	0.3	81.0
Sepiolite-Spot 54	484	17601	1.2	21.7527	6.5	0.0080	7.0	0.0013	2.7	0.39	8.1	0.2	8.0	0.6	3.9	156.1	8.1	0.2	100.5
Sepiolite-Spot 130	1041	16040	0.7	19.7382	5.3	0.0098	5.8	0.0014	2.2	0.39	9.0	0.2	9.9	0.6	225.5	123.3	9.0	0.2	91.3
Sepiolite-Spot 138	244	1243	1.2	22.1781	11.7	0.0088	12.2	0.0014	3.5	0.29	9.1	0.3	8.9	1.1	50.8	286.3	9.1	0.3	102.5
Sepiolite-Spot 28	327	2084	1.0	19.0068	11.7	0.0108	12.1	0.0015	2.9	0.24	9.6	0.3	11.0	1.3	312.1	267.9	9.6	0.3	87.9
Sepiolite-Spot 181	467	7604	1.0	17.0405	9.4	0.0123	9.9	0.0015	3.1	0.32	9.8	0.3	12.4	1.2	555.4	205.8	9.8	0.3	78.9
Sepiolite-Spot 202	249	4354	1.0	16.8876	10.9	0.0125	11.4	0.0015	3.3	0.29	9.9	0.3	12.6	1.4	575.0	236.6	9.9	0.3	78.2
Sepiolite-Spot 60	669	11774	0.8	20.4083	6.8	0.0121	7.0	0.0018	1.9	0.27	11.5	0.2	12.2	0.8	147.8	158.5	11.5	0.2	94.5
Sepiolite-Spot 173	167	1974	0.7	19.9208	10.9	0.0124	11.5	0.0018	3.7	0.32	11.5	0.4	12.5	1.4	204.2	254.0	11.5	0.4	92.2
Sepiolite-Spot 71	1437	14525	1.7	20.4923	4.9	0.0122	5.6	0.0018	2.8	0.50	11.7	0.3	12.4	0.7	138.2	114.1	11.7	0.3	94.8
Sepiolite-Spot 180	333	5651	1.2	20.1635	9.1	0.0125	10.0	0.0018	4.2	0.42	11.8	0.5	12.6	1.3	176.0	213.5	11.8	0.5	93.3
Sepiolite-Spot 8	1086	15812	1.3	20.3260	5.4	0.0126	5.8	0.0019	2.2	0.37	11.9	0.3	12.7	0.7	157.3	125.7	11.9	0.3	94.1
Sepiolite-Spot 82	97	719	0.2	19.2125	16.1	0.0136	16.9	0.0019	4.9	0.29	12.2	0.6	13.7	2.3	287.6	371.1	12.2	0.6	89.0
Sepiolite-Spot 121	183	2947	0.5	15.9648	12.8	0.0164	13.3	0.0019	3.5	0.26	12.2	0.4	16.5	2.2	696.0	273.9	12.2	0.4	74.0
Sepiolite-Spot 200	1350	8345	3.2	17.1377	6.2	0.0153	6.5	0.0019	2.0	0.30	12.2	0.2	15.4	1.0	542.9	135.1	12.2	0.2	79.4
Sepiolite-Spot 154	1091	33337	3.7	19.8479	5.1	0.0132	5.7	0.0019	2.5	0.44	12.2	0.3	13.3	0.8	212.7	118.4	12.2	0.3	91.9
Sepiolite-Spot 109	523	58163	1.3	22.0604	6.3	0.0121	7.0	0.0019	3.2	0.45	12.5	0.4	12.3	0.9	37.9	152.2	12.5	0.4	102.1
Sepiolite-Spot 127	200	1575	1.2	21.3358	9.7	0.0127	10.4	0.0020	3.7	0.35	12.6	0.5	12.8	1.3	42.6	232.7	12.6	0.5	98.8
Sepiolite-Spot 133	336	5443	0.8	18.7491	8.3	0.0144	9.0	0.0020	3.4	0.37	12.6	0.4	14.6	1.3	343.1	188.3	12.6	0.4	86.9
Sepiolite-Spot 170	292	10555	0.5	18.3996	7.3	0.0148	7.7	0.0020	2.6	0.33	12.8	0.3	15.0	1.2	385.5	164.2	12.8	0.3	85.3
Sepiolite-Spot 204	211	2181	1.8	15.4491	14.4	0.0178	14.8	0.0020	3.5	0.24	12.8	0.4	17.9	2.6	765.5	304.7	12.8	0.4	71.7
Sepiolite-Spot 87	340	80347	0.9	20.5273	7.3	0.0134	7.9	0.0020	2.9	0.37	12.8	0.4	13.5	1.1	134.2	172.5	12.8	0.4	95.1
Sepiolite-Spot 20	334	2435	1.2	21.2265	8.3	0.0130	8.7	0.0020	2.3	0.27	12.9	0.3	13.1	1.1	54.8	199.3	12.9	0.3	98.3
Sepiolite-Spot 129	403	5144	0.9	21.4640	8.9	0.0129	9.2	0.0020	2.5	0.27	12.9	0.3	13.0	1.2	28.2	213.6	12.9	0.3	99.4
Sepiolite-Spot 192	140	2307	1.0	19.2515	12.7	0.0144	13.7	0.0020	5.1	0.37	12.9	0.7	14.5	2.0	283.0	290.7	12.9	0.7	89.2
Sepiolite-Spot 166	288	2912	1.5	21.8164	8.9	0.0127	9.4	0.0020	3.0	0.32	12.9	0.4	12.8	1.2	10.9	215.5	12.9	0.4	101.0
Sepiolite-Spot 211	170	8409	1.1	18.1803	9.2	0.0153	9.8	0.0020	3.3	0.34	13.0	0.4	15.4	1.5	412.4	205.5	13.0	0.4	84.3
Sepiolite-Spot 24	1044	40726	0.8	20.1765	5.8	0.0138	6.2	0.0020	2.1	0.34	13.0	0.3	13.9	0.9	174.5	135.6	13.0	0.3	93.4
Sepiolite-Spot 212	316	17767	0.8	18.7020	8.2	0.0149	8.9	0.0020	3.5	0.40	13.0	0.5	15.0	1.3	348.8	185.7	13.0	0.5	86.7
Sepiolite-Spot 47	584	36284	1.4	21.1863	6.1	0.0132	6.5	0.0020	2.1	0.33	13.0	0.3	13.3	0.9	59.4	145.2	13.0	0.3	98.1
Sepiolite-Spot 199	239	7559	0.9	16.0154	10.3	0.0174	10.6	0.0020	2.8	0.26	13.0	0.4	17.5	1.8	689.2	219.8	13.0	0.4	74.3
Sepiolite-Spot 191	476	8833	0.6	19.5517	7.1	0.0143	7.4	0.0020	2.2	0.30	13.0	0.3	14.4	1.1	247.4	163.2	13.0	0.3	90.6
Sepiolite-Spot 50	133	7867	1.4	17.6872	13.5	0.0158	13.9	0.0020	3.7	0.26	13.0	0.5	15.9	2.2	473.5	299.0	13.0	0.5	82.0
Sepiolite-Spot 118	328	46256	1.0	18.8680	7.5	0.0148	8.2	0.0020	3.2	0.39	13.0	0.4	14.9	1.2	328.8	171.5	13.0	0.4	87.4
Sepiolite-Spot 93	308	27140	3.4	21.7230	6.8	0.0129	7.6	0.0020	3.2	0.43	13.1	0.4	13.0	1.0	0.6	165.2	13.1	0.4	100.6
Sepiolite-Spot 120	732	9084	1.6	19.8272	5.4	0.0141	5.9	0.0020	2.3	0.39	13.1	0.3	14.2	0.8	215.1	125.3	13.1	0.3	91.8
Sepiolite-Spot 122	149	3215	1.1	22.1516	10.2	0.0127	10.8	0.0020	3.7	0.34	13.1	0.5	12.8	1.4	47.9	247.9	13.1	0.5	102.5
Sepiolite-Spot 59	671	42844	0.7	19.9313	6.1	0.0141	6.5	0.0020	2.1	0.33	13.1	0.3	14.2	0.9	203.0	141.7	13.1	0.3	92.3
Sepiolite-Spot 53	150	2372	2.0	21.6867	12.9	0.0129	13.4	0.0020	3.6	0.27	13.1	0.5	13.0	1.7	3.5	311.2	13.1	0.5	100.4
Sepiolite-Spot 13	964	18334	1.0	21.3693	5.4	0.0131	5.7	0.0020	2.0	0.35	13.1	0.3	13.3	0.8	38.8	128.3	13.1	0.3	98.9
Sepiolite-Spot 89	148	1039	1.3	15.6499	13.6	0.0179	14.2	0.0020	4.3	0.30	13.1	0.6	18.1	2.5	738.2	288.6	13.1	0.6	72.6
Sepiolite-Spot 114	428	32902	1.0	22.2740	6.5	0.0126	10.4	0.0020	8.1	0.78	13.1	1.1	12.7	1.3	61.3	159.1	13.1	1.1	103.1
Sepiolite-Spot 135	668	56423	1.0	21.0164	5.9	0.0134	6.5	0.0020	2.6	0.40	13.1	0.3	13.5	0.9	78.5	141.2	13.1	0.3	97.3
Sepiolite-Spot 25	244	24515	1.5	21.4099	8.9	0.0131	9.5	0.0020	3.3	0.34	13.1	0.4	13.3	1.3	34.3	214.5	13.1	0.4	99.1
Sepiolite-Spot 158	326	7110	0.7	22.3331	7.5	0.0126	8.1	0.0020	3.0	0.38	13.1	0.4	12.7	1.0	67.8	183.0	13.1	0.4	103.4
Sepiolite-Spot 45	226	36310	1.0	21.0308	8.3	0.0134	8.9	0.0020	3.2	0.36	13.2	0.4	13.5	1.2	76.9	196.3	13.2	0.4	97.4

Table 2. (continued)

Analysis	U (ppm)	$^{206}Pb/^{204}Pb$	U/Th	Isotope ratios: $^{206}Pb^*/^{207}Pb^*$	± (%)	$^{207}Pb^*/^{235}Pb^*$	± (%)	$^{206}Pb^*/^{238}U$	± (%)	Error correlation	Apparent ages: 206Pb*/238U* (Ma)	±1σ (Ma)	207Pb*/235U (Ma)	±1σ (Ma)	206Pb*/207Pb* (Ma)	±1σ (Ma)	Best age (Ma)	±1σ (Ma)	Concordance (%)[a]
Sepiolite-Spot 172	217	13133	1.4	18.4525	11.1	0.0153	11.5	0.0020	3.2	0.28	13.2	0.4	15.4	1.8	379.1	250.0	13.2	0.4	85.5
Sepiolite-Spot 107	159	52772	1.2	18.6254	10.5	0.0152	11.0	0.0021	3.2	0.29	13.2	0.4	15.3	1.7	358.1	237.7	13.2	0.4	86.3
Sepiolite-Spot 152	300	2329	1.0	21.1869	9.8	0.0134	10.4	0.0021	3.4	0.33	13.2	0.5	13.5	1.4	59.3	234.0	13.2	0.5	98.1
Sepiolite-Spot 174	410	44543	1.1	19.5034	7.3	0.0145	7.6	0.0021	2.1	0.28	13.2	0.3	14.7	1.1	253.1	168.6	13.2	0.3	90.4
Sepiolite-Spot 32	263	2372	1.0	21.5616	10.6	0.0132	11.1	0.0021	3.0	0.27	13.3	0.4	13.3	1.5	17.3	256.1	13.3	0.4	99.8
Sepiolite-Spot 110	794	19360	0.9	21.1092	5.6	0.0135	6.1	0.0021	2.3	0.38	13.3	0.3	13.6	0.8	68.1	133.6	13.3	0.3	97.8
Sepiolite-Spot 74	385	9167	0.5	18.9434	5.9	0.0151	6.8	0.0021	3.4	0.50	13.3	0.5	15.2	1.0	319.8	133.5	13.3	0.5	87.8
Sepiolite-Spot 55	282	14620	1.1	19.1171	9.2	0.0149	9.8	0.0021	3.3	0.34	13.3	0.4	15.1	1.5	298.9	210.8	13.3	0.4	88.6
Sepiolite-Spot 119	707	26980	1.3	21.5595	4.9	0.0133	5.4	0.0021	2.3	0.43	13.4	0.3	13.4	0.7	17.6	118.3	13.4	0.3	99.8
Sepiolite-Spot 1	398	4409	0.7	22.0197	5.6	0.0131	6.5	0.0021	3.4	0.51	13.4	0.5	13.2	0.9	33.4	135.8	13.4	0.5	101.9
Sepiolite-Spot 52	168	1715	0.9	17.1881	13.7	0.0167	14.1	0.0021	3.1	0.22	13.4	0.4	16.9	2.4	536.6	301.7	13.4	0.4	79.7
Sepiolite-Spot 86	381	13534	1.0	22.4579	6.1	0.0128	6.5	0.0021	2.4	0.37	13.5	0.3	12.9	0.8	81.4	149.2	13.5	0.3	104.0
Sepiolite-Spot 36	520	7909	0.6	21.5192	5.9	0.0134	6.3	0.0021	2.0	0.32	13.5	0.3	13.6	0.8	22.1	142.7	13.5	0.3	99.6
Sepiolite-Spot 201	361	6534	1.4	20.3153	7.5	0.0143	8.4	0.0021	3.7	0.44	13.5	0.5	14.4	1.2	158.5	176.3	13.5	0.5	94.1
Sepiolite-Spot 148	324	10448	0.9	18.0696	8.5	0.0160	8.9	0.0021	2.7	0.30	13.5	0.4	16.2	1.4	426.0	188.9	13.5	0.4	83.8
Sepiolite-Spot 137	369	5330	0.8	21.2765	7.1	0.0137	7.9	0.0021	3.4	0.43	13.6	0.5	13.8	1.1	49.2	170.5	13.6	0.5	98.5
Sepiolite-Spot 72	272	32560	0.7	18.4712	8.7	0.0158	10.1	0.0021	5.1	0.51	13.6	0.7	15.9	1.6	376.8	195.7	13.6	0.7	85.6
Sepiolite-Spot 177	465	30046	0.6	18.7901	6.6	0.0155	7.0	0.0021	2.3	0.33	13.6	0.3	15.6	1.1	338.2	150.5	13.6	0.3	87.1
Sepiolite-Spot 125	131	1028	1.3	17.3581	13.7	0.0168	14.2	0.0021	3.8	0.27	13.6	0.5	16.9	2.4	514.9	301.6	13.6	0.5	80.5
Sepiolite-Spot 205	674	4011	0.6	21.5036	5.8	0.0136	6.1	0.0021	2.1	0.34	13.6	0.3	13.7	0.8	23.8	138.1	13.6	0.3	99.6
Sepiolite-Spot 179	339	9599	1.1	20.2529	8.0	0.0144	8.5	0.0021	2.6	0.31	13.6	0.4	14.5	1.2	165.7	188.1	13.6	0.4	93.8
Sepiolite-Spot 48	163	6988	0.9	17.6157	12.1	0.0167	12.7	0.0021	3.7	0.29	13.8	0.5	16.8	2.1	482.5	268.4	13.8	0.5	81.7
Sepiolite-Spot 2	136	12404	1.3	22.6201	8.2	0.0130	9.1	0.0021	3.9	0.42	13.8	0.5	13.1	1.2	99.1	202.4	13.8	0.5	104.7
Sepiolite-Spot 96	229	44568	0.8	21.8943	8.8	0.0136	9.6	0.0022	4.0	0.41	13.9	0.6	13.7	1.3	19.5	212.1	13.9	0.6	101.4
Sepiolite-Spot 30	143	2747	1.0	22.0342	10.1	0.0135	10.9	0.0022	3.9	0.36	13.9	0.5	13.6	1.5	35.0	246.8	13.9	0.5	102.0
Sepiolite-Spot 17	134	9637	1.9	17.1867	14.1	0.0173	14.9	0.0022	4.7	0.31	13.9	0.6	17.4	2.6	536.7	310.7	13.9	0.6	79.7
Sepiolite-Spot 171	158	11289	1.1	20.0605	10.4	0.0148	13.3	0.0022	8.3	0.62	13.9	1.1	14.9	2.0	187.9	242.1	13.9	1.1	93.0
Sepiolite-Spot 19	242	20881	1.4	15.3095	9.7	0.0195	10.2	0.0022	3.1	0.31	13.9	0.4	19.6	2.0	784.6	204.0	13.9	0.4	71.1
Sepiolite-Spot 115	580	5841	0.8	21.3232	7.2	0.0140	7.5	0.0022	2.2	0.29	14.0	0.3	14.1	1.1	44.0	172.4	14.0	0.3	98.8
Sepiolite-Spot 95	344	13697	0.9	22.1953	6.4	0.0135	8.0	0.0022	4.9	0.60	14.0	0.7	13.6	1.1	52.7	156.3	14.0	0.7	102.8
Sepiolite-Spot 216	820	36202	1.2	21.3000	4.7	0.0144	5.2	0.0022	2.4	0.46	14.3	0.3	14.5	0.8	46.6	111.5	14.3	0.3	98.7
Sepiolite-Spot 209	75	666	0.6	20.7075	17.8	0.0151	18.4	0.0023	4.7	0.26	14.6	0.7	15.3	2.8	113.6	422.1	14.6	0.7	96.0
Sepiolite-Spot 157	733	15400	0.5	19.7513	5.9	0.0159	6.3	0.0023	2.0	0.31	14.7	0.3	16.1	1.0	224.0	137.5	14.7	0.3	91.6
Sepiolite-Spot 37	459	28395	1.1	21.1552	6.8	0.0150	7.4	0.0023	2.9	0.39	14.8	0.4	15.1	1.1	62.9	161.4	14.8	0.4	98.0
Sepiolite-Spot 187	201	2118	0.4	21.4340	9.4	0.0149	10.1	0.0023	3.7	0.36	15.0	0.5	15.1	1.5	31.6	226.0	15.0	0.5	99.3
Sepiolite-Spot 131	413	4519	0.4	22.1473	7.1	0.0148	7.5	0.0024	2.4	0.33	15.3	0.4	14.9	1.1	47.4	172.1	15.3	0.4	102.6
Sepiolite-Spot 196	349	8529	0.7	21.2957	7.6	0.0154	8.0	0.0024	2.6	0.33	15.3	0.4	15.5	1.2	47.1	181.7	15.3	0.4	98.7
Sepiolite-Spot 128	434	54424	0.6	22.0262	6.5	0.0149	6.8	0.0024	2.2	0.32	15.3	0.3	15.0	1.0	34.1	157.5	15.3	0.3	102.1
Sepiolite-Spot 69	648	7960	1.3	20.9633	5.4	0.0157	5.8	0.0024	2.3	0.40	15.4	0.4	15.8	0.9	84.5	127.4	15.4	0.4	97.2
Sepiolite-Spot 139	888	51609	0.8	20.7392	4.7	0.0160	5.2	0.0024	2.2	0.43	15.5	0.3	16.1	0.8	110.0	111.5	15.5	0.3	96.1
Sepiolite-Spot 203	862	7346	1.1	21.2553	5.1	0.0158	5.4	0.0024	1.7	0.32	15.7	0.3	15.9	0.9	51.6	122.8	15.7	0.3	98.5
Sepiolite-Spot 99	1056	16773	1.2	21.6782	5.2	0.0155	5.5	0.0024	1.8	0.33	15.7	0.3	15.7	0.9	4.4	125.7	15.7	0.3	100.5
Sepiolite-Spot 198	232	62476	0.6	19.8548	7.7	0.0171	8.2	0.0025	2.8	0.34	15.8	0.4	17.2	1.4	211.9	178.3	15.8	0.4	92.1
Sepiolite-Spot 6	646	47357	0.8	20.2739	5.7	0.0167	6.4	0.0025	2.8	0.44	15.8	0.4	16.9	1.1	163.3	133.8	15.8	0.4	94.0
Sepiolite-Spot 34	693	29808	0.5	21.8919	5.0	0.0155	5.6	0.0025	2.5	0.46	15.9	0.4	15.7	0.9	19.3	120.1	15.9	0.4	101.5
Sepiolite-Spot 182	223	4141	0.5	22.6365	8.6	0.0150	9.1	0.0025	3.2	0.35	15.9	0.5	15.2	1.4	100.8	210.4	15.9	0.5	104.9
Sepiolite-Spot 126	205	5415	1.1	19.3074	9.3	0.0177	9.9	0.0025	3.5	0.35	15.9	0.6	17.8	1.8	276.3	213.4	15.9	0.6	89.6
Sepiolite-Spot 175	282	28040	0.5	21.0694	6.8	0.0163	7.4	0.0025	3.1	0.41	16.0	0.5	16.4	1.2	72.6	161.3	16.0	0.5	97.7
Sepiolite-Spot 67	477	9402	1.0	19.8461	7.2	0.0174	7.5	0.0025	2.3	0.30	16.1	0.4	17.5	1.3	212.9	166.6	16.1	0.4	92.1
Sepiolite-Spot 184	185	7384	1.0	19.6058	10.2	0.0178	10.6	0.0025	2.8	0.27	16.3	0.5	17.9	1.9	241.1	235.6	16.3	0.5	91.0
Sepiolite-Spot 111	481	15782	0.6	21.4426	5.6	0.0166	6.0	0.0026	2.1	0.34	16.6	0.3	16.7	1.0	30.6	135.0	16.6	0.3	99.4
Sepiolite-Spot 161	322	17247	1.0	19.8003	6.4	0.0229	6.9	0.0033	2.6	0.38	21.2	0.6	23.0	1.6	218.2	148.2	21.2	0.6	92.1
Sepiolite-Spot 194	332	7704	0.8	20.3925	7.1	0.0239	7.6	0.0035	2.7	0.36	22.7	0.6	24.0	1.8	149.7	165.7	22.7	0.6	94.8

Table 2. (continued)

Analysis	U (ppm)	$^{206}Pb/^{204}Pb$	U/Th	Isotope ratios: $^{206}Pb^*/^{207}Pb^*$	± (%)	$^{207}Pb^*/^{235}Pb^*$	± (%)	$^{206}Pb^*/^{238}U$	± (%)	Error correlation	Apparent ages: 206Pb*/238U* (Ma)	±1σ (Ma)	207Pb*/235U (Ma)	±1σ (Ma)	206Pb*/207Pb* (Ma)	±1σ (Ma)	Best age (Ma)	±1σ (Ma)	Concordance (%)[a]
Sepiolite-Spot 61	214	34936	0.8	19.6764	7.5	0.0250	8.1	0.0036	3.0	0.37	23.0	0.7	25.1	2.0	232.8	173.9	23.0	0.7	91.6
Sepiolite-Spot 11	218	4337	0.7	15.7828	10.2	0.0314	10.7	0.0036	3.0	0.28	23.1	0.7	31.4	3.3	720.3	218.0	23.1	0.7	73.7
Sepiolite-Spot 195	291	4956	0.8	21.1382	7.2	0.0257	7.5	0.0039	2.3	0.31	25.4	0.6	25.8	1.9	64.8	170.6	25.4	0.6	98.4
Sepiolite-Spot 214	2756	47687	2.5	20.9895	2.8	0.0279	3.1	0.0042	1.4	0.45	27.3	0.4	27.9	0.9	81.6	66.2	27.3	0.4	97.8
Sepiolite-Spot 44	457	9798	1.5	21.8010	4.8	0.0269	5.2	0.0043	1.9	0.38	27.4	0.5	27.0	1.4	9.2	115.4	27.4	0.5	101.5
Sepiolite-Spot 43	1862	50896	2.4	21.2204	2.1	0.0281	2.7	0.0043	1.6	0.62	27.8	0.5	28.1	0.7	55.5	49.6	27.8	0.5	98.9
Sepiolite-Spot 142	70	890	1.2	16.9576	15.6	0.0353	16.4	0.0043	5.1	0.31	27.9	1.4	35.2	5.7	566.0	342.1	27.9	1.4	79.3
Sepiolite-Spot 22	1106	96775	1.6	20.8612	3.5	0.0287	4.1	0.0043	2.1	0.50	28.0	0.6	28.8	1.2	96.1	83.7	28.0	0.6	97.2
Sepiolite-Spot 10	1217	51568	1.6	21.5755	3.7	0.0326	4.2	0.0051	2.0	0.47	32.8	0.6	32.6	1.3	15.8	88.6	32.8	0.6	100.7
Sepiolite-Spot 217	542	55170	3.6	20.3461	2.2	0.0829	2.8	0.0122	1.7	0.62	78.4	1.3	80.8	2.2	155.0	51.0	78.4	1.3	96.9
Sepiolite-Spot 215	349	32848	1.0	21.3047	2.9	0.0883	3.2	0.0136	1.4	0.42	87.4	1.2	85.9	2.6	46.1	69.5	87.4	1.2	101.7
Sepiolite-Spot 98	894	193087	1.6	20.5866	2.8	0.0947	3.1	0.0141	1.4	0.44	90.5	1.2	91.8	2.7	127.4	65.6	90.5	1.2	98.5
Sepiolite-Spot 57	807	184708	1.0	20.5684	2.8	0.0991	3.2	0.0148	1.6	0.48	94.6	1.5	95.9	2.9	129.5	66.2	94.6	1.5	98.6
Sepiolite-Spot 149	743	106008	0.9	21.0311	2.2	0.0971	3.1	0.0148	2.1	0.69	94.8	2.0	94.1	2.8	76.8	52.7	94.8	2.0	100.7
Sepiolite-Spot 62	450	27091	1.4	21.3431	3.4	0.1006	4.4	0.0156	2.7	0.63	99.6	2.7	97.3	4.0	41.8	81.2	99.6	2.7	102.3
Sepiolite-Spot 49	851	106286	1.1	20.4615	2.1	0.1064	2.6	0.0158	1.5	0.58	101.0	1.5	102.7	2.5	141.7	48.7	101.0	1.5	98.4
Sepiolite-Spot 70	971	102443	1.0	20.8944	1.8	0.1047	2.6	0.0159	1.9	0.73	101.5	1.9	101.1	2.5	92.3	41.8	101.5	1.9	100.4
Sepiolite-Spot 75	260	29477	0.7	20.2603	2.9	0.1610	3.5	0.0237	1.8	0.52	150.7	2.7	151.6	4.9	164.8	68.8	150.7	2.7	99.4
Sepiolite-Spot 134	825	64765	0.7	20.6060	1.7	0.1600	2.3	0.0239	1.5	0.67	152.3	2.3	150.7	3.2	125.1	40.0	152.3	2.3	101.1
Sepiolite-Spot 9	133	21854	2.0	19.8396	4.2	0.1666	4.5	0.0240	1.7	0.37	152.7	2.5	156.5	6.5	213.7	96.5	152.7	2.5	97.6
Sepiolite-Spot 46	782	63153	1.5	20.4667	2.2	0.1727	3.0	0.0256	2.1	0.68	163.2	3.3	161.8	4.5	141.1	51.7	163.2	3.3	100.9
Sepiolite-Spot 218	1662	151012	1.3	20.2016	1.4	0.1752	2.0	0.0257	1.5	0.74	163.4	2.4	163.9	3.1	171.6	31.9	163.4	2.4	99.7
Sepiolite-Spot 68	828	221889	1.6	19.8518	1.8	0.1811	2.6	0.0261	1.8	0.71	165.9	3.0	169.0	4.0	212.2	41.5	165.9	3.0	98.2
Sepiolite-Spot 153	1648	53782	1.6	20.4317	1.3	0.1764	1.8	0.0261	1.3	0.72	166.3	2.1	165.0	2.8	145.1	29.6	166.3	2.1	100.8
Sepiolite-Spot 40	660	29587	1.0	20.0299	2.1	0.1807	2.8	0.0263	1.9	0.67	167.1	3.2	168.7	4.4	191.5	48.7	167.1	3.2	99.0
Sepiolite-Spot 105	204	38052	0.6	20.2865	2.7	0.1847	3.2	0.0272	1.7	0.54	172.9	2.9	172.1	5.0	161.8	62.6	172.9	2.9	100.4
Sepiolite-Spot 76	535	38777	1.4	19.8925	2.0	0.1888	3.1	0.0272	2.4	0.77	173.3	4.1	175.6	5.0	207.5	45.4	173.3	4.1	98.7
Sepiolite-Spot 102	269	32601	0.9	17.0990	3.2	0.2201	3.9	0.0273	2.2	0.56	173.6	3.7	202.0	7.1	547.9	70.1	173.6	3.7	85.9
Sepiolite-Spot 186	736	55870	1.4	20.1111	2.2	0.1882	2.9	0.0275	1.8	0.63	174.6	3.1	175.1	4.6	182.1	52.1	174.6	3.1	99.7
Sepiolite-Spot 160	527	84954	2.8	11.9551	1.1	0.7180	2.2	0.0623	1.9	0.87	389.4	7.3	549.5	9.5	1284	22	389.4	7.3	70.9
Sepiolite-Spot 106	98	35725	1.9	13.4002	1.4	1.9025	2.4	0.1849	1.9	0.80	1094	19	1082	16	1058	29	1058	29	103.3
Sepiolite-Spot 39	131	53970	1.8	13.3610	1.4	1.8860	2.1	0.1828	1.6	0.75	1082	16	1076	14	1064	28	1064	28	101.7
Sepiolite-Spot 108	175	213107	2.2	13.3220	1.1	1.8890	1.8	0.1825	1.4	0.77	1081	14	1077	12	1070	23	1070	23	101.0
Sepiolite-Spot 112	251	240109	1.8	13.2579	1.3	1.8907	2.2	0.1818	1.8	0.82	1077	18	1078	15	1080	26	1080	26	99.7
Sepiolite-Spot 64	183	228281	2.1	13.2363	1.3	1.9245	2.4	0.1847	2.0	0.84	1093	20	1090	16	1083	25	1083	25	100.9
Sepiolite-Spot 140	250	81528	3.4	13.2093	1.3	1.8875	2.1	0.1808	1.7	0.78	1072	16	1077	14	1087	27	1087	27	98.6
Sepiolite-Spot 220	347	108539	1.9	13.2074	1.1	1.9646	1.8	0.1882	1.4	0.78	1112	14	1103	12	1088	23	1088	23	102.2
Sepiolite-Spot 12	367	67985	1.9	13.1702	1.1	1.9424	1.9	0.1855	1.5	0.80	1097	15	1096	13	1093	23	1093	23	100.4
Sepiolite-Spot 219	57	43490	1.3	13.1678	1.8	1.9682	2.3	0.1880	1.5	0.63	1110	15	1105	16	1094	36	1094	36	101.5
Sepiolite-Spot 147	91	163338	1.9	13.1542	1.6	2.0172	2.6	0.1925	2.0	0.78	1135	21	1121	17	1096	32	1096	32	103.6
Sepiolite-Spot 21	143	123640	2.4	13.1285	1.6	1.9507	2.4	0.1857	1.8	0.74	1098	18	1099	16	1100	33	1100	33	99.9
Sepiolite-Spot 58	604	150012	4.1	13.0275	1.3	1.9448	2.4	0.1838	2.0	0.84	1087	20	1097	16	1115	26	1115	26	97.5
Sepiolite-Spot 31	735	192792	2.6	12.5727	1.2	2.1670	2.2	0.1976	1.8	0.82	1162	19	1171	15	1186	24	1186	24	98.0
Sepiolite-Spot 97	382	899010	2.8	11.4147	1.1	2.7495	2.2	0.2276	1.9	0.86	1322	22	1342	16	1374	21	1374	21	96.2
Sepiolite-Spot 16	163	105412	2.5	11.1074	1.7	3.1639	2.5	0.2549	1.9	0.75	1464	25	1448	19	1426	32	1426	32	102.6
Sepiolite-Spot 188	193	149860	1.2	10.9890	1.2	3.0301	1.8	0.2415	1.3	0.75	1394	17	1415	14	1447	23	1447	23	96.4
Sepiolite-Spot 100	371	64038	1.9	10.9619	1.1	3.1442	2.0	0.2500	1.7	0.85	1438	22	1444	16	1451	20	1451	20	99.1
Sepiolite-Spot 146	249	1053555	2.2	9.6414	1.4	4.2521	2.6	0.2973	2.2	0.84	1678	33	1684	22	1692	26	1692	26	99.2
Sepiolite-Spot 178	751	163139	1.9	9.5392	1.1	3.6097	1.8	0.2497	1.4	0.79	1437	18	1552	14	1711	20	1711	20	84.0
Sepiolite-Spot 104	342	70167	2.8	9.5013	1.2	4.2948	1.9	0.2960	1.5	0.79	1671	22	1692	15	1719	21	1719	21	97.2
Sepiolite-Spot 208	329	50851	1.8	9.4456	1.0	4.3218	1.7	0.2961	1.4	0.79	1672	20	1698	14	1729	19	1729	19	96.7
Sepiolite-Spot 94	156	101462	2.2	9.4367	1.1	4.5198	2.5	0.3093	2.3	0.90	1737	34	1735	21	1731	20	1731	20	100.4
Sepiolite-Spot 193	261	124889	3.1	9.4025	1.2	4.4951	2.2	0.3065	1.9	0.84	1724	28	1730	18	1738	22	1738	22	99.2

10.1002/2016GC006397

Table 2. (continued)

				Isotope ratios							Apparent ages								
Analysis	U (ppm)	$^{206}Pb/^{204}Pb$	U/Th	$^{206}Pb^*/^{207}Pb^*$	± (%)	$^{207}Pb^*/^{235}Pb^*$	± (%)	$^{206}Pb^*/^{238}U$	± (%)	Error correlation	206Pb*/238U* (Ma)	±1σ (Ma)	207Pb*/235U (Ma)	±1σ (Ma)	206Pb*/207Pb* (Ma)	±1σ (Ma)	Best age (Ma)	±1σ (Ma)	Concordance (%)[a]
Sepiolite-Spot 155	282	131141	1.3	9.2606	1.4	4.6093	2.0	0.3096	1.5	0.73	1739	23	1751	17	1766	25	1766	25	98.5
Sepiolite-Spot 164	562	97532	2.7	9.2078	1.1	4.6589	2.4	0.3111	2.1	0.88	1746	33	1760	20	1776	21	1776	21	98.3
Sepiolite-Spot 144	320	216791	2.8	9.1866	1.1	4.5630	2.0	0.3040	1.7	0.84	1711	25	1743	17	1780	20	1780	20	96.1
Sepiolite-Spot 18	1144	78114	4.1	9.1858	0.9	4.5188	1.7	0.3010	1.4	0.84	1697	21	1734	14	1780	16	1780	16	95.3
Sepiolite-Spot 168	470	######	1.6	9.1664	1.3	4.6367	2.2	0.3083	1.8	0.82	1732	28	1756	19	1784	23	1784	23	97.1
Sepiolite-Spot 5	1399	484824	7.7	9.0999	0.9	4.9212	2.1	0.3248	1.9	0.90	1813	30	1806	18	1798	17	1798	17	100.9
Sepiolite-Spot 141	253	89187	1.4	5.6881	1.2	11.6952	2.0	0.4825	1.6	0.81	2538	34	2580	19	2614	19	2614	19	97.1
Sepiolite-Spot 210	143	103107	1.2	5.4295	1.2	13.0312	2.0	0.5132	1.6	0.82	2670	36	2682	19	2691	19	2691	19	99.2
Sepiolite-Spot 101	181	192370	1.6	5.4293	1.2	13.1194	2.3	0.5166	2.0	0.86	2685	43	2688	22	2691	19	2691	19	99.8
Sepiolite-Spot 88	255	194866	0.8	4.8115	1.0	16.4279	1.8	0.5733	1.5	0.84	2921	36	2902	17	2889	16	2889	16	101.1

[a]Filtered to remove discordance >30% or >5% reverse discordance.

10.1002/2016GC006397

Table 3. Trace Element, and O and Hf Isotope Data

Zircon #	$^{206}Pb/^{238}U_a$ age (Ma)	$\pm 1\sigma$ $^{206}Pb/^{238}U$ age (Ma)	Mg (ppm)	P (ppm)	Ti (ppm)	$^{57}Fe/^{30}Si_b$ (ppm)	Y (ppm)	La (ppm)	Ce (ppm)	Pr (ppm)	Nd (ppm)	Sm (ppm)	Eu (ppm)	Gd (ppm)	Tb (ppm)	Dy (ppm)	Ho (ppm)	Er (ppm)	Tm (ppm)	Yb (ppm)	Lu (ppm)	Hf (ppm)	Th (ppm)	U_c (ppm)	$\delta^{18}O$ VSMOW (‰)	$^{176}Hf/^{177}Hf$	εHf	$\varepsilon Hf_{(0)}$ 1σ
5	1.90	0.06	0.0	1693	2	0.00041	3800	0.1	30.2	0.1	1.3	5.9	0.0	46	22	274	113	503	110	1012	218	12685	617	2758	5.56	0.28277	−0.40	0.92
20	8.09	0.30	0.1	267	6	0.00040	1722	0.1	23.6	0.3	5.1	7.2	1.5	33	12	130	50	218	48	428	99	7569	204	177	5.62	0.28233	−6.40	0.89
24	9.78	0.30	0.0	185	6	0.00041	4097	0.2	35.2	0.8	12.1	21.6	0.6	88	33	344	127	517	109	887	180	6053	289	339	5.34	0.28260	−2.36	1.30
8	9.80	0.31	0.1	237	6	0.00038	2259	26.3	124.6	7.7	33.1	13.2	0.3	42	18	197	75	306	62	510	104	5967	167	241	4.34	0.28263	−5.21	0.93
30	10.3	0.3	0.1	251	4	0.00047	989	0.0	36.6	0.0	0.9	1.7	0.3	10	5	64	30	133	33	312	70	9443	238	270	5.31	0.28250	−9.91	0.87
31	12.6	0.5	22.9	5799	11	0.00062	919	55.0	145.6	15.6	69.1	15.8	3.1	22	7	74	28	126	30	301	71	8010	148	189	6.55	0.28227	−17.96	0.89
33	12.6	0.5	0.3	285	8	0.00045	615	0.1	26.9	0.1	1.6	2.1	0.8	9	4	43	19	82	20	196	46	8215	65	106	7.06	0.28234	−15.46	0.91
14	12.8	0.9	4.6	561	9	0.00046	1224	0.1	29.7	0.1	2.4	4.5	1.0	19	7	86	36	154	37	334	75	9430	96	169	6.72	0.28239	−13.73	1.06
7	12.9	2.2	1015.5	294	16	0.00072	778	0.1	27.3	0.1	1.7	3.1	0.9	12	5	55	22	104	24	245	55	8065	72	110	7.03	0.28236	−14.74	1.11
18	13.1	0.5	1.1	280	5	0.00048	748	0.1	31.8	0.1	1.2	2.3	0.7	11	4	50	21	103	25	252	60	8984	83	149	9.77	0.28238	−13.96	0.76
29	13.2	1.2	0.8	297	6	0.00046	643	0.2	33.6	0.1	1.2	2.0	0.5	9	4	43	18	84	21	196	48	9327	78	150	7.39	0.28254	−14.00	0.81
3	13.2	0.5	0.1	283	9	0.00043	814	0.1	31.5	0.2	2.6	3.5	1.0	15	5	63	24	106	24	225	53	8781	104	112	7.07	0.28252	−9.00	0.91
1	13.2	0.4	0.0	363	7	0.00039	1603	0.1	51.4	0.3	5.2	7.6	2.2	30	12	121	48	203	46	416	94	9285	189	211	7.02	0.28241	−13.10	0.84
12	13.3	0.5	6.8	370	5	0.00058	3905	0.1	114.2	0.5	8.3	15.7	3.3	75	30	336	131	557	117	1018	208	8788	678	540	5.45	0.28251	−9.61	0.95
13	13.3	0.5	1.9	812	9	0.00059	1131	4.5	46.2	1.6	8.6	5.7	1.2	21	8	86	35	153	35	317	76	9507	149	165	6.61	0.28233	−15.73	0.79
2	13.3	0.5	0.4	348	7	0.00047	942	0.1	28.5	0.1	1.8	3.0	0.9	13	6	66	27	127	30	295	73	8604	78	135	7.07	0.28237	−14.50	0.94
28	13.7	0.5	0.0	284	8	0.00044	665	0.1	26.4	0.1	1.5	2.9	0.9	12	4	48	19	83	20	188	46	8072	71	97	6.93	0.28271	−16.75	0.76
16	13.8	0.4	0.3	1352	3	0.00044	2429	4.0	22.5	1.1	3.9	4.5	1.3	29	13	169	75	342	80	738	165	10458	100	442	7.72	0.28233	−15.88	0.96
21	13.9	0.5	0.8	293	9	0.00042	1177	0.1	34.9	0.3	3.9	6.5	1.7	24	9	91	35	146	33	297	69	8579	124	125	5.99	0.28260	−12.44	1.11
25	14.1	0.4	0.1	294	2	0.00044	1541	0.0	20.9	0.0	0.6	2.2	0.2	16	8	100	47	210	52	490	112	10764	191	470	5.75	0.28242	−8.51	0.86
32	14.7	0.9	0.5	247	7	0.00048	452	0.1	20.0	0.0	0.9	1.5	0.6	7	3	32	13	61	14	152	38	9146	39	71	6.30	0.28235	−15.19	0.96
11	18.1	1.0	0.8	376	13	0.00046	1154	0.1	29.9	0.3	3.5	5.2	1.5	22	9	88	35	141	32	294	64	7498	78	65	6.20	0.28248	−10.26	1.13
15	22.3	0.7	0.1	233	4	0.00045	1930	0.1	68.8	0.3	5.1	9.1	2.1	36	14	150	60	255	61	561	127	9989	565	531	7.79	0.28251	−9.27	0.95
6	25.8	0.8	0.5	256	5	0.00047	1868	0.1	48.1	0.4	5.8	9.7	2.3	39	13	142	55	225	48	418	91	8813	239	232	7.56	0.28238	−13.60	1.01
17	98.9	3.0	0.1	149	3	0.00045	725	0.0	30.9	0.0	0.7	1.5	0.4	8	3	44	20	96	26	289	76	10249	200	511	5.66	0.28260	−4.29	0.81
9	166	5	0.3	271	7	0.00040	1453	0.4	26.7	0.2	3.8	6.5	1.7	25	9	102	40	183	41	389	92	9322	214	275	5.47	0.28243	−9.01	0.99
22	168	5	136.1	350	68483	0.20488	1234	0.2	18.2	0.1	1.3	2.7	0.5	16	7	83	37	172	39	377	86	8561	96	239	4.86	0.28238	−2.31	1.00

Table 3. (continued)

Zircon #	$^{206}Pb/^{238}U_a$ age (Ma)	$\pm 1\sigma$ $^{206}Pb/^{238}U$ age (Ma)	Mg (ppm)	P (ppm)	Ti (ppm)	$^{57}Fe/^{30}Si_b$ (ppm)	Y (ppm)	La (ppm)	Ce (ppm)	Pr (ppm)	Nd (ppm)	Sm (ppm)	Eu (ppm)	Gd (ppm)	Tb (ppm)	Dy (ppm)	Ho (ppm)	Er (ppm)	Tm (ppm)	Yb (ppm)	Lu (ppm)	Hf (ppm)	Th (ppm)	U_c (ppm)	$\delta^{18}O$ VSMOW (‰)	$^{176}Hf/^{177}Hf$	εHf	$εHf_{(0)}$ 1σ
26	185	6	0.3	178	8	0.00047	713	0.1	21.2	0.0	0.8	1.7	0.2	9	4	44	20	93	23	247	60	11980	342	728	6.81	0.28261	−9.47	0.82
19	261	9	0.6	278	9	0.00047	1311	0.1	11.0	0.2	2.9	4.7	0.9	20	8	90	40	188	40	395	94	9439	103	263	4.74	0.28293	10.93	1.08
23	825	25	2.6	599	15	0.00091	3930	0.2	32.7	1.0	14.4	19.7	1.0	89	33	344	127	498	104	870	177	8937	486	806	5.59	0.28293	−1.28	0.74
4	1064	32	0.4	666	9	0.00046	1560	0.1	2.1	0.2	2.9	5.3	0.2	31	12	138	52	205	41	345	69	10571	59	223	7.86	0.28225	5.00	1.15
27	1904	57	0.0	458	10	0.00043	1154	0.0	14.4	0.1	2.2	4.5	0.2	23	9	97	36	145	30	263	54	10033	191	326	7.31	0.28223	0.90	0.80
10	2733	83	0.1	291	15	0.00041	921	0.1	16.2	0.6	8.4	8.0	2.5	28	8	80	29	113	23	203	46	7873	44	38	5.84	0.28110	2.73	0.83

[a]Age after ^{207}Pb common Pb correction ($^{207}Pb/^{206}Pb = 0.8283$).
[b]Relative measure for beam overlap with Fe-bearing phases (which are typically also elevated in Ti); max. value on 91500 reference zircon 5×10^{-4}.
[c]Concentration from trace element analysis ($U^+/^{30}SiO^+$ relative to NIST610 standard with 457.1 ppm U).
[d]Hf data notes:
1 Data reduction methodology is from *Woodhead et* al. [2004].
2 Analytical methods described in detail by *Gehrels and Pecha* [2014].
3 $(^{176}Yb + ^{176}Lu)/^{176}Hf$ (%) expresses the proportion of ^{176} due to $^{176}Yb + ^{176}Lu$ versus the proportion due to ^{176}Hf, in %.
4 Volts Hf is the sum of voltages of all Hf isotopes.
5 $^{176}Hf/^{177}Hf$ is the measured $^{176}Hf/^{177}Hf$, corrected for fractionation and interfences. Shown with uncertainty expressed at 1-sigma.
6 $^{176}Lu/^{177}Hf$ is the intensity of ^{176}Lu, calculated from the measured instensity of ^{175}Lu and $^{176}Lu/^{175}Lu = 0.02653$ (from *Patchett*, 1983, compared to the measured intensity of ^{177}Hf. Fractionation of Lu isotopes is assumed to be the same as fractionation of Yb isotopes.
7 $^{176}Hf/^{177}Hf$ (T) is the $^{176}Hf/^{177}Hf$ corrected to the time of crystallization using a decay constant of $1.867e^{-11}$ (from *Scherer et al.*, 2001 and *Soderland et al.*, 2004)
8 E-Hf (0) is the present-day epsilon Hf value using $^{176}Hf/^{177}Hf = 0.282785$ and $^{176}Lu/^{177}Hf = 0.0336$ (from *Bouvier et al.*, 2008). The uncertainty is expressed at 1-sigma.
9 E-Hf (T) is the epsilon Hf value at the time of crystallization. The uncertainty is expressed at 1-sigma.
10 U-Pb ages are based on 206/238 for ages younger than ~1.0 Ga, and on 206/207 for ages older than ~1.0 Ga. This age cutoff may be slightly different for each sample.
11 Isotope ratios as follows:
180/177 1.88666 *Patchett* [1983]
179/177 0.7325 *Patchett and Tatsumoto* [1980]
178/177 1.46718 *Patchett* [1983]
176/177 0.28216 *Patchett* [1983]
174/177 0.00871 *Patchett* [1983]
176/175 0.02653 *Patchett* [1983]
176/171 0.901691 *Vervoort et al.* [2004]
173/171 1.1323569 *Vervoort et al.* [2004]
172/171 1.531736 *Vervoort et al.* [2004]
12 CHUR is from *Bouvier et al.* [2008], using $^{176}Hf/^{177}Hf = 0.282785$ and $^{176}Lu/^{177}Hf = 0.0336$.

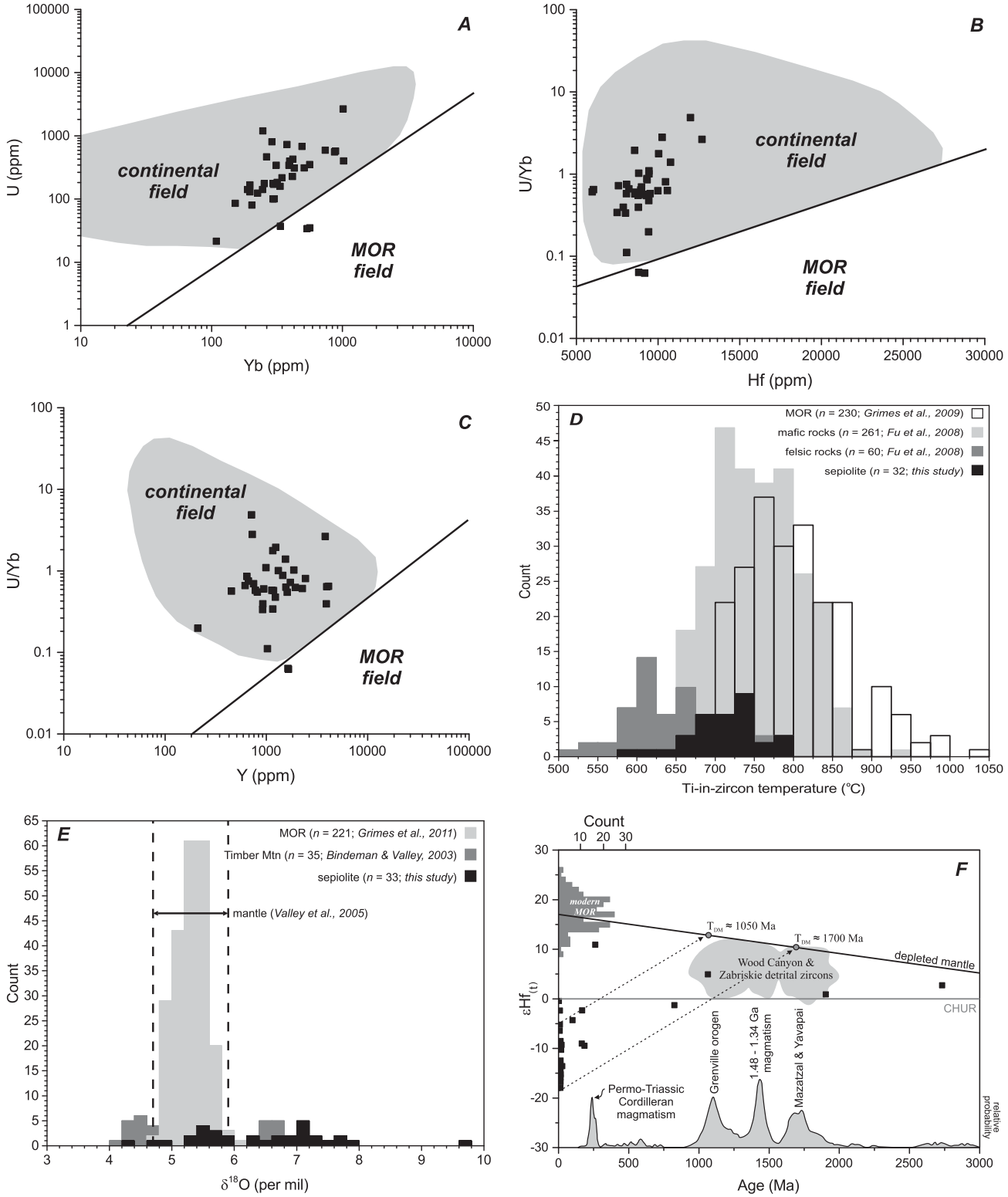

Figure 4. (a–c) Selected trace element discriminant diagrams for continental and mid-ocean ridge (MOR) zircons adapted from *Grimes et al.* [2007, 2015]. (d) Histogram of Ti-in-zircon crystallization temperatures for zircons from felsic and mafic rocks [*Fu et al.*, 2008], MOR gabbros [*Grimes et al.*, 2009], and sepiolite. (e) Histogram of $\delta^{18}O$ values for zircons from the Timber Mountain caldera complex [*Bindeman and Valley*, 2003], MOR gabbros [*Grimes et al.*, 2011], and sepiolite (analytical error of 0.23‰). (f) $\varepsilon Hf_{(t)}$ versus age diagram showing the distribution of sepiolite (black squares) compared to detrital zircons in the Proterozoic Wood Canyon Formation and Cambrian Zabriskie Quartzite Formation [*Gehrels and Pecha*, 2014]. Depleted mantle model of *Workman and Hart* [2005]. The age distribution of southern Cordilleran detrital zircons is shown at the base—peaks represent major zircon-forming events [*Gehrels and Pecha*, 2014]. The histogram depicts the distribution of whole-rock εHf values of modern MOR rocks from the Mid-Atlantic Ridge [*Thomas*, 2013].

source of detrital zircon at the sepiolite location in the Amargosa Desert. TMCC tuffs of the Paintbrush and Timber Mountain Groups are the regionally most abundant units. Published U-Pb zircon ages [*Bindeman et al*., 2006] range between 12.4 and 13.5 Ma (Paintbrush) and 11.7 and 12.0 Ma (Timber Mountain). Among Miocene sepiolite zircons, Paintbrush (72%) dominates over Timber Mountain (9%) with the remainder being likely derived from poorly dated pre-Paintbrush deposits [*Byers et al*., 1976]. Identical δ^{18}O compositions (6–7‰) for Miocene sepiolite and TMCC zircons [*Bindeman and Valley*, 2003] further support this provenance. The youngest sepiolite zircon population averages 1.89 ± 0.04 Ma ($n = 5$; mean square of weighted deviates MSWD = 0.70; Figure 3c). Based on age, elevated U abundance, and overlapping εHf$_{(0)}$, these zircons are correlated with old pre-caldera Glass Mountain rhyolites from Long Valley caldera, California [*Sarna-Wojcicki et al*., 2005; *Simon et al*., 2014], ~250 km to the NW of the sepiolite location. Quaternary zircons <1.89 Ma are absent in the sepiolite, which agrees with a post-2 Ma southward shift of the Amargosa River depocenter from the Amargosa Desert to the Tecopa Basin [*Morrison*, 1999]. Pre-middle Miocene zircon crystals in the sepiolite are likely related to the Eagle Mountain Formation interpreted as being recycled from various sources: Oligocene volcanics in the Death Valley region, the Late Cretaceous Sierra Nevada batholith, and the Late Jurassic Hunter Mountain batholith [*Niemi*, 2013]. Regional sources for older zircons are known, and for ca. 1.1 Ga ages comprise the Neoproterozoic Pahrump Group and Stirling Quartzite Formation, and the Neoproterozoic-Cambrian Wood Canyon Formation, as well as the Stirling Quartzite and Cambrian Johnnie and Zabriskie Quartzite formations for ca. 1.4, 1.7, 2.7 Ga ages [*Niemi*, 2013]. A single sepiolite zircon with a Permo-Triassic age potentially corresponds to Triassic sedimentary remnants in Utah and Nevada (Figure 4f) [*Gehrels and Pecha*, 2014].

5.2. Recognition and Mitigation of Zircon Contamination

In addition to standard shipboard and laboratory sample handling procedures, the following steps may reduce the likelihood of contamination by drilling mud, or to be able to identify contaminating zircons:

1. Avoidance of cores and intervals that are heavily fractured or obviously disturbed.
2. Whole-rock analyses by shipboard ICP or portable X-ray fluorescence spectrometry of intervals for Zr content. Zircon contamination is probably more significant in low Zr, zircon-poor intervals.
3. Collection and analysis of the drilling mud used during drilling.
4. Removal of uneven surfaces on the margin of the core, although this will reduce the volume of sample available.
5. Thorough scrubbing and washing (aided by ultrasound) of core samples before crushing.
6. Where possible, analyze zircons in situ in polished petrographic thin sections.
7. Careful comparison of magmatic or depositional ages with independent age estimates (e.g., shipboard age-model, magnetostratigraphy). Ages significantly younger, older, or more diverse than expected, should be treated with caution.
8. Addition of δ^{18}O, trace element, and εHf analyses on dated zircons. Our results demonstrate that sepiolite-derived zircons are continental in origin.
9. Careful consideration of ages 1.9 Ma, 12–15 Ma, ca. 95 Ma, ca. 150–170 Ma, ca. 1.1 Ga, ca. 1.7 Ga, and ca. 2.7 Ga.

6. Conclusions

Sea Mud™ (sepiolite) contains significant quantities of zircon predominantly derived from middle Miocene intracontinental silicic volcanics, but a wide range of other sources is involved. Collectively, zircon trace element, δ^{18}O, and εHf compositions classify essentially all sepiolite zircons as continental, although individual chemical or isotopic identifiers might not always be unique. Divergence of zircon ages from shipboard age-models and age heterogeneity can be a warning for contamination, especially for igneous or primary volcanic (i.e., tephra fall) rocks with typically near-unimodal zircon age distributions. Moreover, zircons in MOR and other primitive magmatic compositions are likely to be distinguishable from sepiolite-derived zircons by a combination of trace element and isotopic (e.g., O, Hf) analyses; therefore, wherever possible, these should be measured in conjunction with U-Pb ages. In contrast, marine sedimentary and volcaniclastic deposits, including pyroclastic density current deposits, are likely to include a diverse population of detrital zircons entrained during transport, and therefore have polymodal zircon distributions. Because these can be partly or entirely derived from continental sources, sepiolite contamination remains a concern for such

samples. In this case, the analyzed zircon age populations should be compared to the sepiolite age peaks reported here. Zircons analyzed in situ (e.g., in petrographic sections), in contrast, are assumed to be trustworthy.

Acknowledgments
We thank the captain and crew of the R/V JOIDES Resolution and the scientific and technical staff of International Ocean Discovery Program [IODP] Expedition 350 for help in collecting samples. Funds from a U.S. Science Support Program/Consortium for Ocean Leadership Post-Expedition Awards to Andrews, Schmitt, and Busby, and National Science Foundation award HRD-1137774 (Andrews, Brown) facilitated this study. The ion microprobe facility at UCLA is partly supported by a grant from the Instrumentation and Facilities Program, Division of Earth Sciences, National Science Foundation. The authors are unaware of any conflicts of interest. All data used to support our conclusions are included in this paper. We thank Mark Pecha for conducting the Hf analyses at the University of Arizona, Arizona LaserChron Center, which is supported by the National Science Foundation NSF-EAR award 1338583. Constructive reviews by Kelsie Dadd, Bruno Dhuime, an anonymous reviewer, and editor Janne Blichert-Toft improved this paper greatly.

References

Andrews, G. D. M., A. K. Schmitt, C. J. Busby, and S. R. Brown (2015), Geochronology and geochemistry of zircons from the IODP Site U1437 in the rear of the Izu-Bonin Volcanic Arc, *AGU Fall Meeting*, San Francisco, Calif.

Bindeman, I. N., and J. W. Valley (2003), Rapid generation of both high- and low-δ^{18}O, large volume silicic magmas at Timber Mountain/Oasis Valley caldera complex, Nevada, *Geol. Soc. Am. Bull.*, *115*, 581–595.

Bindeman, I. N., A. K. Schmitt, and J. W. Valley (2006), U-Pb zircon geochronology of silicic tuffs from the Timber Mountain/Oasis Valley caldera complex, Nevada: Rapid generation of large volume magmas by shallow-level remelting, *Contrib. Mineral. Petrol.*, *152*, 649–665.

Byers, F. M., W. J. Carr, P. P. Orkild, W. D. Quinlivan, and K. A. Sargent (1976), Volcanic suites and related cauldrons of Timber Mountain-Oasis Valley caldera complex, southern Nevada, *U.S. Geol. Surv. Prof. Pap. 919*, pp. 1–70.

Carr, M. D., D. A. Sawyer, K. Nimz, F. Maldonado, and W. C. Swadley (1996), Digital bedrock geologic map database of the Beatty 30 × 60-minute quadrangle, *U.S. Geol. Surv. Open File Rep., 96-291*, Nevada, Calif.

Clift, P. D., A. Carter, U. Nicholson, and H. Masago (2013), Zircon and apatite thermochronology of the Nankai Trough accretionary prism and trench, Japan: Sediment transport in an active and collisional margin setting, *Tectonics*, *32*, 377–395.

Ferry, J. M., and E. B. Watson (2007), New thermodynamic models and revised calibrations for the Ti-in-zircon and Zr-in-rutile thermometers, *Contrib. Mineral. Petrol.*, *154*(4), 429–437.

Fu, B., F. Z. Page, A. J. Cavosie, J. Fournelle, N. T. Kita, J. S. Lackey, S. A. Wilde, and J. W. Valley (2008), Ti-in-zircon thermometry: Applications and limitations, *Contrib. Mineral. Petrol.*, *156*, 197–215.

Gehrels, G., and M. Pecha (2014), Detrital zircon U-Pb geochronology and Hf isotope geochemistry of Paleozoic and Triassic passive margin strata of western North America, *Geosphere*, *10*, 49–65.

Gehrels, G. E., V. A. Valencia, and J. Ruiz (2008), Enhanced precision, accuracy, efficiency, and spatial resolution of U-Pb ages by laser ablation-multicollector-inductively coupled plasma-mass spectrometry, *Geochem. Geophys. Geosyst.*, *9*, Q03017, doi:10.1029/2007GC001805.

Graber, K. K., E. Pollard, B. Jonasson, and E. Schulte (2002), Overview of Ocean Drilling Program engineering tools and hardware. *Proc. Ocean Drill. Program Tech.*, *31*, doi:10.2973/odp.tn.31.2002.

Grimes, C. B, B. E. John, P. B. Kelemen, F. Mazdab, J. L. Wooden, M. J. Cheadle, K. Hanghøj, and J. J. Schwartz (2007), The trace element chemistry of zircons from oceanic crust: A method for distinguishing detrital zircon provenance, *Geology*, *35*, 643–646, doi:10.1130/G23603A.1.

Grimes, C. B., B. E. John, M. J. Cheadle, F. K. Mazdab, J. L. Wooden, S. Swapp, and J. J. Schwartz (2009), On the occurrence, trace element geochemistry, and crystallization history of zircon from in situ ocean lithosphere, *Contrib. Mineral. Petrol.*, *158*, 757–783.

Grimes, C. B., T. Ushikubo, B. E. John, and J. W. Valley (2011), Uniformly mantle-like δ^{18}O in zircons from oceanic plagiogranites and gabbros, *Contrib. Mineral. Petrol.*, *161*, 13–33.

Grimes, C. B., T. Ushikubo, R. Kozdon, and J. W. Valley (2013), Perspectives on the origin of plagiogranite in ophiolites from oxygen isotopes in zircon, *Lithos*, *179*, 48–66.

Grimes, C. B., J. L. Wooden, M. J. Cheadle, and B. E. John (2015), "Fingerprinting" tectono-magmatic provenance using trace elements in igneous zircon, *Contrib. Mineral. Petrol.*, *170*, 1–26.

Hosterman, J. W., and S. H. Patterson (1992), Bentonite and Fuller's Earth Resources of the United States, *U.S. Geol. Surv. Prof. Pap. 1522*, 1–50.

House, C. H., B. A. Cragg, A. Teske, and the Leg 201 Scientific Party (2003), Drilling contamination tests during ODP Leg 201 using chemical and particulate tracers, in *Proc. Ocean Drill. Program Initial Rep., 201*, edited by S. L. D'Hondt et al., pp. 1–19. [Available at http://iodp.tamu.edu/tools/.]

Huey, P. E. (2009), IODP drilling and coring technology—Past and present, *Final Rep. PN119160*, pp. 18, Stress Eng. Services Inc., Houston, Tex. [Available at http://www.iodp.org/doc_download/3464-iodp-drilling-coring-tech-final.]

Jutzeler, M., J. D. White, P. J. Talling, M. McCanta, S. Morgan, A. Le Friant, and O. Ishizuka (2014), Coring disturbances in IODP piston cores with implications for offshore record of volcanic events and the Missoula megafloods, *Geochem. Geophys. Geosyst.*, *15*, 3572–3590.

Kidd, R. B. (1978), Core discing and other drilling effects in DSDP Leg 42A Mediterranean sediment cores, *Initial Rep. D. S. D. P.*, *42*, pp. 1143–1149, doi:10.2973/dsdp.proc.42-1.app1.1978.

Leggett, J. K. (1982), Drilling-induced structures in Leg 66 cores, *Init. Rep. D. S. D. P.*, *66*, pp. 531–538.

Lever, M. A., M. Alperin, B. Engelen, F. Inagaki, S. Nakagawa, B. O. Steinsbu, A. Teske, and IODP Expedition 301 Scientists (2006), Trends in Basalt and Sediment Core Contamination During IODP Expedition 301, *Geomicrobio. J.*, *23*, 517–530.

Minor, S. A., et al. (1993), Preliminary geologic map of the Pahute Mesa 30′ × 60′ quadrangle, Nevada, *U. S. Geol. Surv. Open-File Rep. 93-299*.

Monteleone, B. D., S. L. Baldwin, L. E. Webb, P. G. Fitzgerald, M. Grove, and A. K. Schmitt (2007), Late Miocene-Pliocene eclogite facies metamorphism, D'Entrecastreaux Islands, SE Papua New Guinea, *J. Metamorph. Geol.*, *25*, 245–265.

Morrison, R. B. (1999), Lake Tecopa: Quaternary geology of Tecopa Valley, California, a multimillion-year record and its relevance to the proposed nuclear-waste repository at Yucca Mountain, Nevada, in L. Wright and B. Troxel, Cenozoic Basins of the Death Valley region, *Geol. Soc. Am. Spec. Pap. 333*, pp. 301–344.

Niemi, N. A. (2013), Detrital zircon age distributions as a discriminator of tectonic versus fluvial transport: An example from the Death Valley, USA, extended terrane, *Geosphere*, *9*, 126–137.

Paces, J. B., and J. D. Miller (1993), Precise U-Pb ages of Duluth complex and related mafic intrusions, northeastern Minnesota: Geochronological insights to physical, petrogenetic, paleomagnetic, and tectonomagmatic processes associated with the 1.1 Ga midcontinent rift system, *J. Geophys. Res.*, *98*, 13,997–14,013.

Sambridge, M. S., and W. Compston (1994), Mixture modeling of multi-component data sets with application to ion-probe zircon ages, *Earth Planet. Sci. Lett.*, *128*, 373–390.

Sarna-Wojcicki, A. M., et al. (2005), Tephra Layers of Blind Spring Valley and Related Upper Pliocene and Pleistocene Tephra Layers, California, Nevada, and Utah: Isotopic Ages, Correlation, and Magnetostratigraphy, *U.S. Geol. Surv. Prof. Pap. 1701*, 1–63.

Schmitt, A. K., M. Grove, T. M. Harrison, O. Lovera, J. Hulen, and M. Walters (2003), The Geysers-Cobb Mountain Magma System, California (Part 1): U-Pb zircon ages of volcanic rocks, conditions of zircon crystallization and magma residence times, *Geochim. Cosmochim. Acta*, *67*, 3423–3442.

Schwartz, J. J., B. E. John, M. J. Cheadle, E. A. Miranda, C. B. Grimes, J. L. Wooden, and H. J. Dick (2005), Dating the growth of oceanic crust at a slow-spreading ridge, *Science*, *310*, 654–657.

Shinjoe, H., T. Nakajima, Y. Orihashi, S. Saito, H. Oda, and T. Danhara (2014), Zircon U-Pb ages of tuffs and volcaniclastic sandstone of the core sample of IODP Exp. 322 at the Northern Part of the Shikoku Basin, *AGU Fall Meeting Abstracts 1*, 4927.

Simon, J. I., D. Weis, D. J. DePaolo, P. R. Renne, R. Mundil, and A. K. Schmitt (2014), Assimilation of preexisting Pleistocene intrusions at Long Valley by periodic magma recharge accelerates rhyolite generation: Rethinking the remelting model, *Contrib. Mineral. Petrol.*, *167*, 1–34.

Smith, D. C., A. J. Spivack, M. R. Fisk, S. A. Haveman, and H. Staudigel (2000a), Tracer based estimates of drilling-induced microbial contamination of deep sea crust, *Geomicrobiol. J.*, *17*, 207–219.

Smith, D. C., A. J. Spivack, M. R. Fisk, S. A. Haveman, H. Staudigel, H., and Leg 185 Shipboard Scientific Party (2000b), Methods for quantifying potential microbial contamination during deep ocean coring, *O. D. P. Tech. Note 28*.

Thomas, C. (2013), Hafnium isotope geochemistry of the gabbroic crust sampled along the Mid-Atlantic Ridge: Constraints on the nature of the upper mantle, unpublished MS thesis, pp. 112, Ohio Univ., Athens, Ohio.

Trail, D., S. J. Mojzsis, T. M. Harrison, A. K. Schmitt, E. B. Watson, and E. D. Young (2007), Constraints on Hadean zircon protoliths from oxygen isotopes, Ti-thermometry, and rare earth elements, *Geochem. Geophys. Geosyst.*, *8*, doi:10.1029/2006GC001449.

USGS (2006), Shuttle Radar Topography Mission, 1 Arc Second mosaic. Filled finished 2.0 Global Land Cover Facility, Univ. of Maryland, College Park, Md.

Valley, J. W., et al. (2005), 4.4 billion years of crustal maturation: oxygen isotope ratios of magmatic zircon, *Contrib. Mineral. Petrol.*, *150*, 561–580.

Wiedenbeck, M., et al. (2004), Further characterisation of the 91500 zircon crystal, *Geostand. Geoanal. Res.*, *28*, 9–39.

Workman, R. K., and S. R. Hart (2005), Major and trace element composition of the depleted MORB mantle (DMM), *Earth Planet. Sci. Lett.*, *231*, 53–72.

Yanagawa, K., et al. (2013), The first microbiological contamination assessment by deep-sea drilling and coring by the D/V Chikyu at the Iheya North hydrothermal field in the Mid-Okinawa Trough (IODP Expedition 331), *Front. Microbiol.*, *4*, 1–10, doi:10.3389/fmicb.2013.00327.